6-3-2017

First Na Lidar Measurements of Turbulence Heat Flux, Thermal Diffusivity, and Energy Dissipation Rate in the Mesopause Region

Yafang Guo
Embry-Riddle Aeronautical University

Alan Z. Liu
Embry-Riddle Aeronautical University, liuz2@erau.edu

Chester S. Gardner
University of Illinois at Urbana-Champaign

Guo, Y., Liu, A. Z., & Gardner, C. S. (2017). First Na Lidar Measurements of Turbulence Heat Flux, Thermal Diffusivity, and Energy Dissipation Rate in the Mesopause Region. *Geophys. Res. Lett., 44*(11). https://doi.org/10.1002/2017GL073807

AGU PUBLICATIONS

Geophysical Research Letters

RESEARCH LETTER
10.1002/2017GL073807

Key Points:
- Turbulence-induced vertical heat flux in the mesopause is directly measured with a Na Doppler lidar
- Eddy thermal diffusivity and turbulent energy dissipation rate are derived
- Dynamical heating/cooling by both waves and turbulence is determined

Supporting Information:
- Supporting Information S1

Correspondence to:
A. Z. Liu,
alan.liu@erau.edu

Citation:
Guo, Y., A. Z. Liu, and C. S. Gardner (2017), First Na lidar measurements of turbulence heat flux, thermal diffusivity, and energy dissipation rate in the mesopause region, *Geophys. Res. Lett.*, *44*, 5782–5790, doi:10.1002/2017GL073807.

Received 12 APR 2017
Accepted 18 MAY 2017
Accepted article online 22 MAY 2017
Published online 3 JUN 2017

First Na lidar measurements of turbulence heat flux, thermal diffusivity, and energy dissipation rate in the mesopause region

Yafang Guo[1], Alan Z. Liu[1,2], and Chester S. Gardner[2]

[1]Center for Space and Atmospheric Research and Department of Physical Sciences, Embry-Riddle Aeronautical University, Daytona Beach, Florida, USA, [2]Department of Electrical and Computer Engineering, University of Illinois at Urbana-Champaign, Urbana, Illinois, USA

Abstract Turbulence is ubiquitous in the mesopause region, where the atmospheric stability is low and wave breaking is frequent. Measuring turbulence is challenging in this region and is traditionally done by rocket soundings and radars. In this work, we show for the first time that the modern Na wind/temperature lidar located at Andes Lidar Observatory in Cerro Pachón, Chile, is able to directly measure the turbulence perturbations in temperature and vertical wind between 85 and 100 km. Using 150 h of lidar observations, we derived the frequency (ω) and vertical wave number (m) spectra for both gravity wave and turbulence, which follow the power law with slopes consistent with theoretical models. The eddy heat flux generally decreases with altitude from about -0.5 Km s^{-1} at 85 km to -0.1 Km s^{-1} at 100 km, with a local maximum of -0.6 Km s^{-1} at 93 km. The derived mean turbulence thermal diffusivity and energy dissipation rate are 43 m^2 s^{-1} and 37 mW kg^{-1}, respectively. The mean net cooling resulted from the heat transport and energy dissipation is -4.9 ± 1.5 K d^{-1}, comparable to that due to gravity wave transport at -7.9 ± 1.9 K d^{-1}. Turbulence key parameters show consistency with turbulence theories.

1. Introduction

Vertical transport by turbulence plays a fundamental role in establishing the thermal structure, composition, and circulation of the mesosphere/lower thermosphere (MLT) below the turbopause [e.g., *Akmaev*, 2001; *Qian et al.*, 2009; *Zhu et al.*, 2010; *Garcia et al.*, 2016; *Meraner and Schmidt*, 2016]. Turbulence is generated by wave breaking in the MLT through mechanisms such as convective and dynamic instabilities [e.g., *Hodges*, 1969; *Lindzen*, 1981; *Zhao et al.*, 2003; *Liu et al.*, 2004; *Williams et al.*, 2006; *Hecht et al.*, 2014]. This transport process is described as a mixing effect characterized by diffusion coefficients (also called diffusivity). Many studies have contributed to our knowledge of turbulence and its influence on the atmosphere. It is difficult to directly measure turbulence in the upper atmosphere because the turbulent eddies are small, with scales ranging from a few tens of meters to a few kilometers, and the temperature, wind, and density fluctuations associated with them are too small to be observed from instruments. For the same reason, most atmospheric models cannot resolve turbulence-scale motions, except with direct numerical simulation [*Fritts et al.*, 2014].

The energy cascade process of turbulence is characterized by energy dissipation rate ε, a measure of how fast energy is dissipated to molecular scale. The transports of constituents, heat, momentum, and their mixing effects along with the process are represented by the diffusion coefficients often denoted as k_{zz}, k_H, and k_M, respectively. Until now, only the diffusion coefficient for inert constituents (k_{zz}) and turbulent energy dissipation rate (ε) have been measured, primarily by in situ observations of neutral density fluctuations and their power spectra such as rocket-borne ionization gauges [e.g. ,*Lübken*, 1997; *Das et al.*, 2009], by observations of the expansion of chemiluminescent trails released by rockets [e.g., *Bishop et al.*, 2004], and by measuring the spectral broadening of radar pulses caused by turbulence-induced wind fluctuations [e.g., *Fukao et al.*, 1994; *Hocking*, 1996]. The ionization gauge and radar techniques use turbulence theory to relate the observations to k_{zz} and ε, while the rocket trail technique is a direct measurement of the turbulent mixing of constituents. The thermal (k_H) and momentum (k_M) diffusion coefficients are usually inferred from k_{zz} by ignoring chemical effects and so that $k_H \approx k_{zz}$ and by assuming a value for the turbulence Prandtl number Pr so $k_M = k_H/Pr = k_{zz}/Pr$. Because of the large variabilities of these turbulence parameters [*Lübken et al.*, 1987], there is still considerable uncertainty about their values in the MLT.

In this paper we show the first direct measurements of turbulence heat flux and the associated thermal diffusion coefficient with a narrowband Na wind and temperature lidar located at Andes Lidar Observatory (ALO) in Cerro Pachón, Chile, (30.25°S, 70.74°W). The 150 h of lidar data from 19 nights of observations is used to derive the turbulence fluctuations associated with temperature and vertical wind. Turbulence heat flux and thus k_H are derived to characterize the heat transport and heating/cooling effect by turbulence. Energy dissipation rate and associated heating are also calculated. These are also compared with the heat flux from dissipating gravity wave (GW) derived from the same data set. The capability to simultaneously measure both the wave- and turbulence-induced heat transport processes can provide important insights on the relationship between wave breaking and turbulence generation and their combined effects on the thermal balance of the mesopause region.

2. Key Parameters of Turbulence

Turbulence transport is usually modeled as a diffusive process, a larger-scale analogue of molecular diffusion. The vertical turbulence flux of sensible heat ($\overline{w'T'}$) is defined as the covariance between vertical wind (w') and temperature (T') perturbations induced by turbulence, where the primes denote perturbations and the overbar denotes sample average over a period of time. The thermal diffusion coefficient k_H is defined in terms of the potential temperature θ as

$$\overline{w'\theta'} = -k_H \frac{\partial \bar{\theta}}{\partial z} = -k_H \left(\Gamma_{\text{ad}} + \frac{\partial \bar{T}}{\partial z} \right) \frac{\bar{\theta}}{\bar{T}}, \tag{1}$$

where $\Gamma_{\text{ad}} = g/C_p$ is the dry adiabatic lapse rate and θ is defined as

$$\theta = T(p_0/p)^{R/C_p}, \tag{2}$$

and p is the atmospheric pressure, $p_0 = 1000$ hPa, $R = 287$ m^2 K^{-1} s^{-2} is the gas constant for dry air, $C_p = 1003$ m^2 K^{-1} s^{-2} is the specific heat at constant pressure, and $g = 9.5$ m s^{-2} is the gravitational acceleration at the mesopause. By linearizing equation (2), multiplying by w', we have

$$\frac{\overline{w'\theta'}}{\bar{\theta}} = \frac{\overline{w'T'}}{\bar{T}} - \frac{R}{C_p} \frac{\overline{w'p'}}{\bar{p}}. \tag{3}$$

For turbulence, since $\overline{\theta'^2}/\overline{\theta^2} \approx \overline{T'^2}/\overline{T^2}$ [*Tatarskii*, 1971; *Gavrilov et al.*, 2005], we assume that the second term on the right is negligible [*Becker and Schmitz*, 2002]. Hence, with equation (1), k_H can be expressed as

$$k_H \approx -\frac{\overline{w'T'}}{\Gamma_{\text{ad}} + \partial \bar{T}/\partial z} = -\frac{g}{N^2} \frac{\overline{w'T'}}{\bar{T}}, \tag{4}$$

where the squared buoyancy frequency N^2 is

$$N^2 = \frac{g}{\bar{T}} \left(\frac{\partial \bar{T}}{\partial z} + \frac{g}{C_p} \right). \tag{5}$$

Thus, k_H can be calculated from measured $\overline{w'T'}$.

In addition to $\overline{w'T'}$, the variance profiles of w' and T' ($\overline{w'^2}$ and $\overline{T'^2}$) can also be directly calculated from lidar measurements. These quantities have been applied to estimate turbulence parameters in observations based on turbulence theories [e.g., *Gavrilov et al.*, 2005; *Clayson and Kantha*, 2008; *Alexander and Barnet*, 2007; *Zhang et al.*, 2012]. Here we can use the variances and the turbulence heat flux measured from lidar to verify the consistency between them. *Weinstock* [1981] showed that for stably stratified turbulence, ε can be related to the variance of w' as

$$\varepsilon = C_0 \overline{w'^2} N, \tag{6}$$

where C_0 is a dimensionless constant with a theoretical value of $C_0 \approx \alpha^{-3/2} \approx 0.5$ and $\alpha \approx 1.5$ is the Kolmogorov constant.

With the assumption of $k_H \approx k_{zz}$, ε can be related to k_H according to *Weinstock* [1978] as

$$k_H \approx \frac{\pi^{1/2}}{4C_0}\frac{\varepsilon}{N^2}. \tag{7}$$

The variance of relative temperature perturbation $\overline{T'^2}$ is also related to ε according to *Gardner and Liu* [2016]

$$\frac{\overline{T'^2}}{\bar{T}^2} \approx \frac{4N}{g^2}\varepsilon. \tag{8}$$

Using these equations, we can then derive ε from equation (6) and compare the measured $\overline{w'^2}$ and $\overline{T'^2}$ with those predicted by equations (7) and (8).

Similar to dissipating gravity waves, turbulent mixing also transports heat downward, which generally cools the atmosphere. The associated heating rate is

$$-\frac{1}{\bar{\rho}}\frac{\partial(\bar{\rho}\overline{w'T'})}{\partial z} \tag{9}$$

and can be combined with the heating rate due to turbulence energy dissipation ε/C_p to derive the net heating or cooling of the atmosphere caused by turbulence.

3. Data Processing

The ALO Na Doppler lidar located in Cerro Pachón, Chile, uses the three-frequency technique [*Krueger et al.*, 2015] to measure line-of-sight wind, temperature, and Na density. The design architecture and performance specifications for this instrument are summarized in *Liu et al.* [2016]. For this study we employed 150 h of observations acquired during 19 nights when the lidar was pointed exclusively at zenith. The nights cover campaigns on May 2014 (two nights), August 2014 (four nights), September 2014 (seven nights), and January 2015 (six nights). Photon count signals were obtained at a temporal resolution of 6 s and a vertical resolution of 25 m. The procedures to derive turbulence fluctuations T' and w' are described in detail by *Gardner and Liu* [2014], and we describe it briefly here. The system equations that relate the photon counts to temperature and wind are linearized, with the background quantities obtained by low-pass filtering the photon counts with a 2-D Hamming window (2.5 min and 500 m full width at half maximum) to retain fluctuations at gravity wave scales larger than 5 min and 1 km, which are chosen based on the knowledge that the smallest GW vertical (and horizontal) wavelengths are ~1 km and the highest frequencies are near buoyancy frequencies in the mesopause region [*Blix et al.*, 1990; *Gardner et al.*, 1993; *Lu et al.*, 2015]. The residual counts are regarded as turbulence fluctuations and used to derive T' and w' based on an inversion of the linearized system equations. An improvement was made from *Gardner and Liu* [2014] by considering the system equations for temperature and wind metrics [*Papen et al.*, 1995] only, without Na density. The inversion matrix is more robust, and the contaminations by large perturbations in Na densities due to sporadic Na layers are eliminated. A detailed method description and explanations for choosing 1 km and 5 min as separation scales are given in the supporting information.

Even though the signal levels acquired by the ALO Na lidar are high, at these high resolutions required to resolve the turbulence fluctuations, the photon noise errors (Δw and ΔT) are still much larger than w' and T'. For example, the root-mean-square (RMS) of w' is about 2 m s^{-1}, while the RMS photon noise errors are 10 − 12 m s^{-1}. However, since we are interested in measuring the second-order statistics of w' and T' (viz., covariance and variances), not their instantaneous values, the significant photon noise can be reduced by averaging long enough data to reduce the uncertainties of these statistics to acceptable levels.

Because the wind and temperature are derived from the same set of signals, their photon noises are correlated, which introduces a significant bias to their covariance. This bias, however, can be easily eliminated by cross multiplying measured temperature and vertical wind perturbations, $T' + \Delta T'$ and $w' + \Delta w$, at two consecutive samples instead of from the same sample [*Gardner and Liu*, 2014], because the photon noises at two different times are uncorrelated. Variances of w' and T' are also calculated with the same approach. A trade-off of this approach is the time resolution reduced by a factor of 2 with an effective resolution of 12 s.

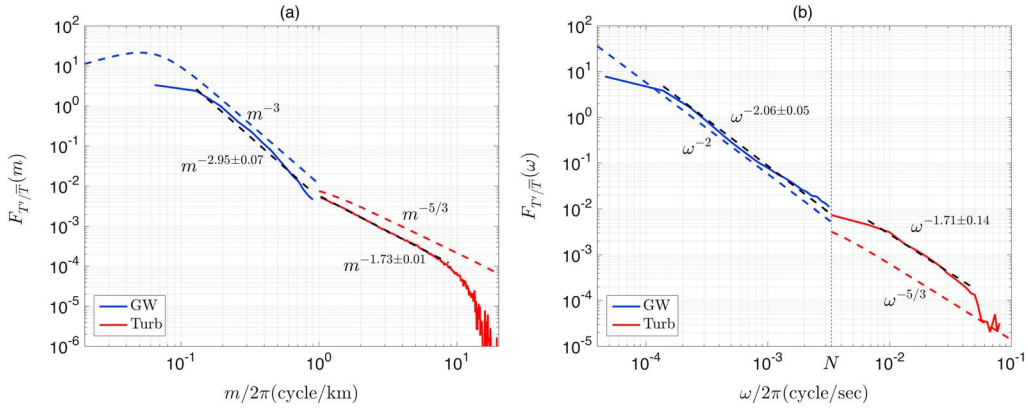

Figure 1. (a) Vertical wave number (m) and (b) temporal frequency (ω) spectra of relative temperature perturbations due to gravity waves (blue) and turbulence (red). Blue and red dashed lines represent the spectra predicted from theoretical models; solid lines are measured from high-resolution lidar measurements; black dashed lines represent the data used for fitting.

Although this technique eliminates the photon noise biases from the heat flux and variance calculations, unbiased photon noise is still the dominant error source for the measurements reported here. The uncertainties (in standard deviations) are

$$\begin{aligned}
\mathrm{Std}(\Delta w'T') &= \sqrt{\frac{\Delta z \Delta t}{2L\tau}}\mathrm{Std}(\Delta w)\mathrm{Std}(\Delta T),\\
\mathrm{Std}(\Delta T'^2) &= \sqrt{\frac{2\Delta z \Delta t}{L\tau}}\mathrm{Var}(\Delta T),\\
\mathrm{Std}(\Delta w'^2) &= \sqrt{\frac{2\Delta z \Delta t}{L\tau}}\mathrm{Var}(\Delta w),
\end{aligned} \tag{10}$$

where $L = 2.5$ km is the vertical resolution of the final smoothed profiles and $\tau = 150$ h is the averaging period, while $\Delta z = 100$ m and $\Delta t = 6$ s are the sample resolutions of the turbulence heat flux and variances. Note that the factor of 2 arises in the heat flux uncertainty because two instantaneous heat flux estimates can be derived from the two sets of w' and T' values measured during the adjacent time bins.

4. Turbulence Power Spectra

Several theoretical models have been developed for the gravity wave spectra, including the linear stability [*Dewan and Good*, 1986], Doppler spreading theory [*Hines*, 1991], and the diffusive theory [*Weinstock*, 1990]. There are numerous observations of gravity wave spectra made with a variety of techniques including balloon-borne sensors in the troposphere and lower stratosphere [e.g., *Zhang et al.*, 2006], mesosphere-stratosphere-troposphere radar [e.g., *Fritts et al.*, 1988], VHF radar [e.g., *VanZandt et al.*, 1991; *Larsen et al.*, 1987], and Na lidar [e.g., *Senft and Gardner*, 1991] in the mesosphere. Here we show that the Na lidar can extend the spectra measurement into the turbulence scales.

The high-resolution ALO Na lidar measurements cover the ranges of frequency (ω) and vertical wave number (m) that include both gravity wave and turbulence scales. The temporal and vertical resolutions are 60 s and 500 m for gravity waves and 6 s and 25 m for turbulence. The ω spectrum was calculated from temperature perturbations on each night averaged from all altitudes, and the m spectrum was calculated in the 85–100 km altitude range for each profile then averaged for the entire night. Figure 1 shows the comparison between theoretical spectra (dashed colored lines) from theoretical models [*Gardner and Liu*, 2014] and the observational spectra (solid colored lines) from lidar measured fluctuations (i.e. relative temperature fluctuations). The observed spectra were averaged from all nightly mean spectra after the noise floors were subtracted. Slopes and their uncertainties were estimated by linear regression. Black dashed lines represent the data points applied to the linear fitting. The buoyancy frequency N ($\sim 2\pi/5$ min) in the ω spectra plot represents the separation between gravity waves and turbulence.

The gravity wave spectra agree well with the theoretical m^{-3} and ω^{-2} power laws, with the slope for ω slightly steeper than the theoretical value. In the turbulence spectra, the noise floor starts at about 10 km^{-1} (or 100 m)

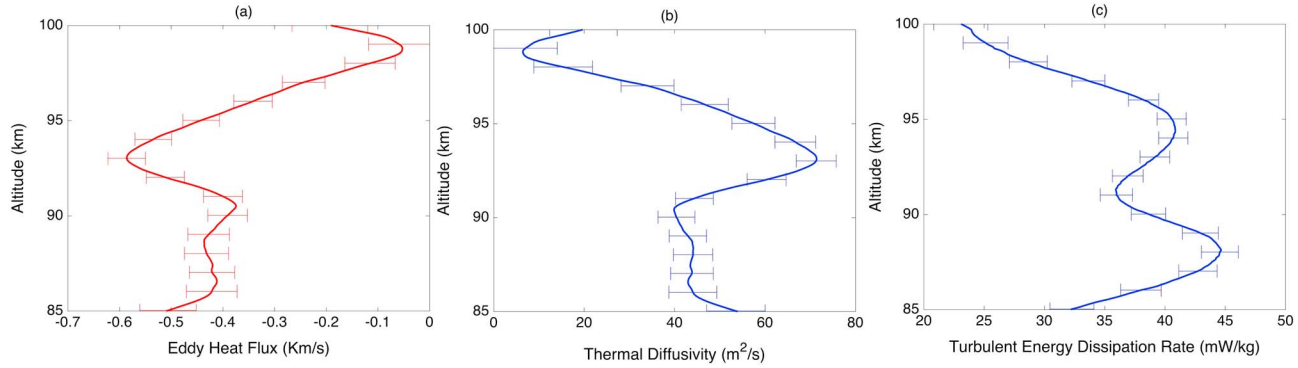

Figure 2. (a) Vertical eddy heat flux, (b) thermal eddy diffusion coefficient k_H, and (c) energy dissipation rate ε calculated from lidar measurements.

in the m spectrum and 0.05 s^{-1} (or 20 s) in the ω spectrum. Both turbulence m spectrum and ω spectrum are consistent with the theoretical value of $-5/3$ with slopes of -1.73 ± 0.01 and -1.71 ± 0.14, respectively. Overall, there is a good agreement between the measured and theoretical spectra. The fact that the slopes can be clearly identified in the turbulence scales indicates that the ALO Na lidar is sensitive to turbulence perturbations and can detect them well above the noise floor.

5. Turbulence Heat Flux and Thermal Diffusion Coefficient

The measured turbulence heat flux $\overline{w'T'}$ is shown in Figure 2a. It is negative throughout the region, indicating that turbulent mixing transports heat downward. The magnitude in general decreases with increasing altitude from about -0.5 Km s^{-1} at 85 km to -0.1 Km s^{-1} at 100 km, with a local maximum at 93 km of -0.6 Km s^{-1}. The k_H profile shown in Figure 2b also exhibits a general decrease with increasing altitude, from 52 m^2 s^{-1} at 85 km to 10 m^2 s^{-1} at 100 km, with a local maximum of 71 m^2 s^{-1} at 93 km. These measured k_H values are generally consistent with the k_{zz} values measured by other techniques in other latitudes [e.g., *Lübken*, 1997; *Das et al.*, 2009; *Bishop et al.*, 2004] and larger than the k_{zz} values used in WACCM (Whole Atmosphere Community Climate Model) which has a maximum of about 20 m^2 s^{-1} [*Smith*, 2012, Figure 7]. ε was calculated based on equation (6) and is shown in Figure 2c. The average ε between 85 and 100 km is about 37 mW kg^{-1}, which corresponds to an average heating rate of about 3.2 K d^{-1}.

With the measured variances, we can examined the suitable value of C_0 in equation (6). We calculated the variances $\overline{w'^2}$ and $\overline{T'^2}$ predicted by equations (7) and (8) using k_H in Figure 2b and compared them with directly measured variances. The Brunt-Väisälä frequency is calculated with the mean temperature by equation (5). We found that when the theoretical value $C_0 = 0.5$ was used, the predicted variances are too small compared with observed values. *Weinstock* [1981] obtained an empirical value of $C_0 = 0.37$ based on experimental data from *Heck et al.* [1977]. We also found that using $C_0 = 0.37$ gives a better agreement with the measured variances. The results are plotted in Figure 3. Overall, the agreement is good for both $\overline{T'^2}$ and $\overline{w'^2}$, and the differences are

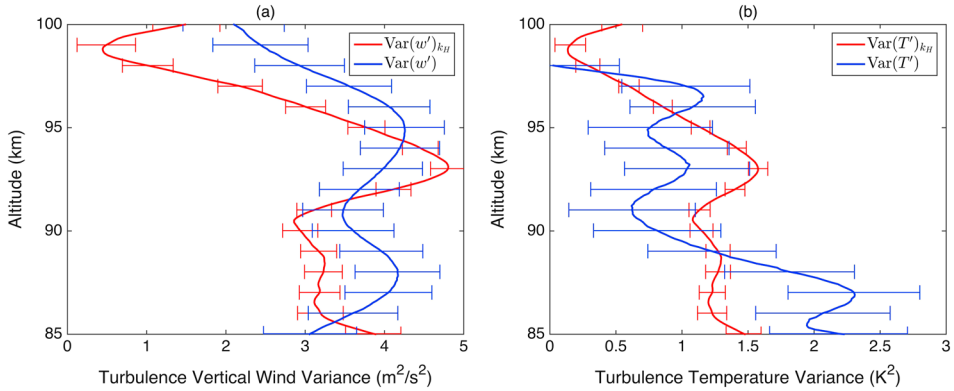

Figure 3. (a) Turbulence-induced vertical wind variance and (b) turbulence-induced temperature variance measured from lidar observations (blue) and calculated using the k_H values (red) in Figure 2b and equation (8) with a C_0 value of 0.37.

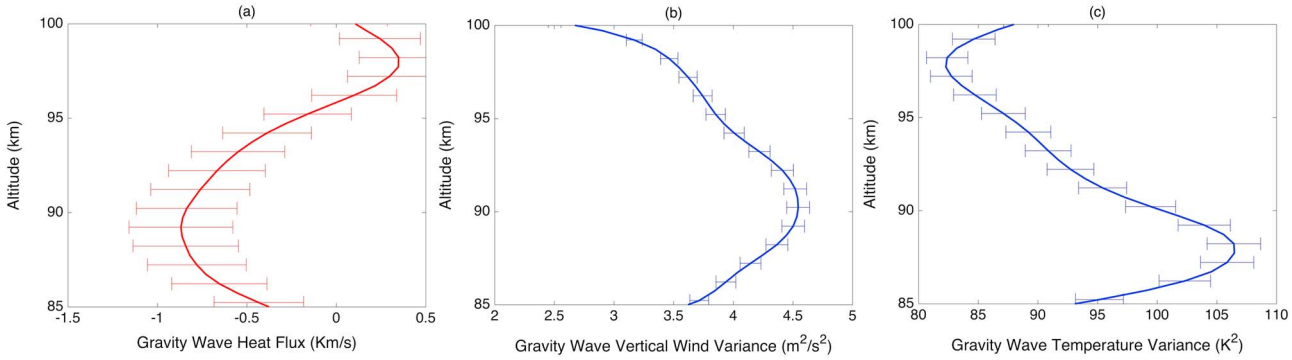

Figure 4. (a) Vertical gravity wave heat flux, (b) wave-induced vertical wind variance and (c) wave-induced temperature variance computed from the same lidar measurements used to derive the turbulence parameters shown in Figure 2.

smallest around 93 km where the flux and k_H are the largest. Our observation therefore supports the notion that the actual C_0 is likely less than 0.5 for the mesopause region.

To place the turbulence measurements in perspective, the profiles of gravity wave-induced heat flux, wind, and temperature variances were also calculated from the same data set and plotted in Figure 4. As expected the gravity wave sensible heat flux is also downward [*Walterscheid*, 1981]. Its magnitude is similar to the eddy heat flux, but the profile shape is different. The gravity wave heat flux increases from about −0.4 Km s^{-1} at 85 km, reaching a maximum of about −0.9 Km s^{-1} near 89 km and then decreases to essentially zero above 96 km. This behavior is similar to that observed at the Starfire Optical Range, NM (35.0°N, 106.5°W) [*Gardner and Liu*, 2007]. The wave- and turbulence-induced vertical wind variances (Figures 3a and 4b) are comparable, but the wave-induced temperature variance (Figure 4c) is about 50 times larger than the turbulence-induced variance (Figure 3b). Although the magnitudes of temperature variances are much different, the overall profiles are similar. Both temperature variances exhibit maximum near 87 and 88 km and minimum above 96 km. This is probably related to the convective or static stability of the atmosphere, which is generally more stable above the mesopause where the vertical temperature gradient becomes positive. The turbulence-induced temperature perturbations are strongest at about the same altitude range where wave activity is the most energetic and are weakest where wave activity is the least energetic, which is consistent with the notion that turbulence is mostly generated by wave breaking.

In terms of the thermal effect of turbulence, it is well known that the turbulent energy deposition induces a heating to the background atmosphere. By using in situ rocket measurements, *Lübken* [1997] found out that the heating rates corresponding to energy dissipation rate ε are stronger in summer mesopause and much smaller in winter, varying from 1 K d^{-1} to 10∼20 K d^{-1}. He also pointed out that this heating has to be compensated by other cooling mechanisms. While the cooling effect caused by gravity wave downward heat transport has been studied with simulations and observations [e.g., *Gardner and Yang*, 1998; *Gardner and Liu*, 2007; *Hickey et al.*, 2011], the cooling caused by turbulence has only been estimated by a few numerical simulations [*Liu*, 2000; *Zhu et al.*, 2010]. Our results show that the downward heat flux induced by turbulence induces a significant cooling effect to the MLT as well. Shown in Figure 5 are the cooling/heating rates due to turbulence and gravity wave heat transport (equation (9)) and turbulent energy dissipation. The flux convergence associated with turbulence heat transport results in a cooling of the atmosphere with an average of −8.1 K d^{-1}. This cooling more than balances the heating caused by turbulent energy dissipation of about

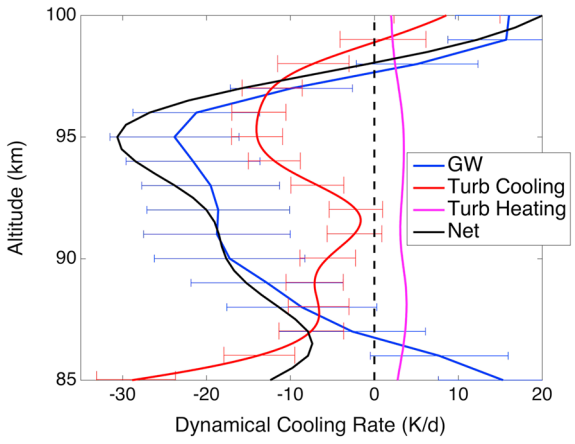

Figure 5. Atmospheric heating/cooling rates associated with vertical heat transport by turbulence (equation (9)) and waves.

3.2 K d^{-1} so that the total effect of turbulence is a cooling of the mesopause region of −4.9 K d^{-1}. Wave-induced heat transport also causes a more significant cooling between 87.5 and 98 km. However, the large wave flux convergence below 87.5 km results in a strong heating of the atmosphere. Thus, the net effect of gravity waves and turbulence between 85 and 100 km is primarily dynamical cooling, with a maximum of about −32 K d^{-1} near 95 km and a mean of −12.8 K d^{-1}.

6. Conclusion

The transport of heat, momentum, and constituents by turbulence diffusion in the MLT region plays a very significant role in establishing the general circulation and thermal structure of atmosphere. It is well recognized that different chemical species are well mixed by this eddy diffusion process below turbopause, and the eddy diffusivity k_{zz} is the same for all species. Currently, numerous ground-based and in situ observational techniques estimate k_{zz} indirectly from measuring the energy dissipation rate (ϵ) with uncertainties remain in estimating ϵ and determining the dependence of k_{zz} on ϵ. These uncertainties can affect the measurements of k_{zz} by 2–3 orders of magnitude [*Vlasov and Kelley*, 2014, 2015]. Also, the discrepancies between these observational coefficients and coefficients used in general circulation models suggest the necessity for a more effective way to determine k_{zz}.

In this paper we showed that the Na wind/temperature lidar at ALO is now capable of detecting turbulence-scale perturbations and providing direct measurements of the eddy heat flux and thermal diffusion coefficient k_H. For the first time, k_H is directly derived from eddy heat transport. Other key parameters such as the energy dissipation rate and the associated heating rate are also derived from the measurements without resorting to complex turbulence theory. The measured k_H has an average of 43 m^2 s^{-1} and a maximum of 72 m^2 s^{-1} at 93 km, and generally decreases with altitude above, which is consistent with some other results of k_{zz} measured by balloons and rockets. These results could provide significant references for the gravity wave parameterization in general circulation models such as WACCM, in which the k_{zz} varies between 10 and 20 m^2 s^{-1} in the mesopause region [*Smith*, 2012], much less than our results.

Another advantage of this high-resolution lidar technique is that both turbulence and gravity waves perturbations can be measured at the same time so that the transport induced by gravity wave and turbulence can be easily compared, as well as the characteristics of both gravity waves and turbulence (i.e., variance). Our results suggest that the downward heat fluxes are comparable for waves and turbulence, and the corresponding net cooling rate of 12.8 K d^{-1} can bring substantial cooling effects to the mesopause region, which was only studied by numerical simulations before.

The spectral analysis, along with the temperature and wind variance, that confirmed the consistency between measured turbulent parameters and turbulence theory, also suggests that the value of the undetermined constant C_0 in the turbulence theory is likely to be smaller than the theoretical value of 0.5, supporting the value of 0.37 suggested by *Weinstock* [1981]. Note that it is not possible to have a clear-cut separation between gravity waves and turbulence. In this analysis, our choice of 1 km is based both on past observational studies and our spectral analysis (Figure 1a). Furthermore, the turbulence outer scale, estimated using equation (7) in *Gardner and Liu* [2014] with our derived energy dissipation rate of about 40 mW/kg (Figure 2c) and $N^2 = 4 \times 10^{-4}$ s^{-2}, is about 700 m, which is consistent with the 1 km breakpoint between gravity waves and turbulence. These results further prove that the lidar measurements can indeed capture at least a large portion of turbulence fluctuations. This is an important advancement that will enable the studies of neutral atmosphere turbulence processes and gravity wave dynamics and their impacts on the atmosphere in the MLT region.

Characterizing turbulence from observations has always been a challenge due to the large variation of gravity wave activities. The turbulent parameters also exhibit strong seasonal variations [e.g., *Lübken*, 1997; *Hall et al.*, 1999; *Sasi and Vijayan*, 2001]. Thus, relatively long averaging periods (~100 h) are necessary to measure turbulence parameters, especially the second-order statistics such as flux and variance. The current ALO Na lidar is equipped with 70 cm diameter telescopes and with a power-aperture product of 0.6 W m^2, which is typical for modern lidar systems. Here in this work, we only use 150 h observational data on 19 nights. With more data acquired through different seasons in the future, the results are expected to vary. By employing larger telescope receiving systems with efficient optical designs [*Smith and Chu*, 2015] and higher power lasers, the required averaging times and uncertainties can be reduced substantially, and the data will have a more complete coverage of turbulence spectra. The current results show that even existing lidar systems are

now capable of characterizing the seasonal variations of the vertical eddy heat transport and the diffusion coefficient and its impacts on the thermal balance in the mesopause region.

Finally, assuming that the turbulence fluctuations are approximately isotropic, the radial wind variance would be comparable to the vertical wind variance. Therefore, our results also indicate that it is possible for existing Doppler lidars to measure turbulence momentum flux and turbulent Prandtl number by using off-zenith measurements to retrieve turbulence horizontal wind perturbations with the same data processing technique used in this study.

Acknowledgments
The Na lidar at ALO is part of the Consortium of Resonance and Rayleigh Lidars, supported by the National Science Foundation (NSF) Geospace Facilities program via grants AGS-1136278 and AGS-1136208. The University of Illinois at Urbana-Champaign, Department of Electrical and Computer Engineering provided funds for the ALO building construction. The recent lidar system upgrade and subsequent campaign was supported by the NSF Major Research Instrument grant AGS-1229085. A. Liu and Y. Guo are partially supported by NSF grants AGS-1110199 and AGS-1115249 and the National Natural Science Foundation of China (grant 41274154). C. Gardner's work is partially supported by NSF grant AGS-1115725. We are grateful for the excellent support provided by the Cerro Pachón astronomy facility managed by the Association of Universities for Research in Astronomy. The routine ALO Na Lidar data between 80 and 105 km and contour plots are available at http://lidar.erau.edu/data/nalidar/. The processed turbulence and gravity wave parameters presented in this paper are available upon request.

References

Akmaev, R. A. (2001), Simulation of large-scale dynamics in the mesosphere and lower thermosphere with the doppler-spread parameterization of gravity waves 2. Eddy mixing and the diurnal tide, *J. Geophys. Res.*, *106*(D1), 1205–1213.

Alexander, M. J., and C. Barnet (2007), Using satellite observations to constrain parameterizations of gravity wave effects for global models, *J. Atmos. Sci.*, *64*(5), 1652–1665.

Becker, E., and G. Schmitz (2002), Energy deposition and turbulent dissipation owing to gravity waves in the mesosphere, *J. Atmos. Sci.*, *59*(1), 54–68, doi:10.1175/1520-0469(2002)059<0054:EDATDO>2.0.CO;2.

Bishop, R. L., M. F. Larsen, J. H. Hecht, A. Z. Liu, and C. S. Gardner (2004), TOMEX: Mesospheric and lower thermospheric diffusivities and instability layers, *J. Geophys. Res.*, *109*, D02S03, doi:10.1029/2002JD003079.

Blix, T. A., E. V. Thrane, and Ø. Andreassen (1990), In situ measurements of the fine-scale structure and turbulence in the mesosphere and lower thermosphere by means of electrostatic positive ion probes, *J. Geophys. Res.*, *95*(D5), 5533–5548, doi:10.1029/JD095iD05p05533.

Clayson, C. A., and L. Kantha (2008), On turbulence and mixing in the free atmosphere inferred from high-resolution soundings, *J. Atmos. Oceanic Technol.*, *25*(6), 833–852, doi:10.1175/2007JTECHA992.1.

Das, U., H. S. S. Sinha, S. Sharma, H. Chandra, and S. K. Das (2009), Fine structure of the low-latitude mesospheric turbulence, *J. Geophys. Res.*, *114*, D10111, doi:10.1029/2008JD011307.

Dewan, E. M., and R. E. Good (1986), Saturation and the "universal" spectrum for vertical profiles of horizontal scalar winds in the atmosphere, *J. Geophys. Res.*, *91*(D2), 2742–2748, doi:10.1029/JD091iD02p02742.

Fritts, D. C., T. Tsuda, S. Kato, T. Sato, and S. Fukao (1988), Observational evidence of a saturated gravity wave spectrum in the troposphere and lower stratosphere, *J. Atmos. Sci.*, *45*(12), 1741–1759, doi:10.1175/1520-0469(1988)045<1741:OEOASG>2.0.CO;2.

Fritts, D. C., K. Wan, J. Werne, T. Lund, and J. H. Hecht (2014), Modeling the implications of Kelvin-Helmholtz instability dynamics for airglow observations, *J. Geophys. Res. Atmos.*, *119*, 8858–8871, doi:10.1002/2014JD021737.

Fukao, S., M. D. Yamanaka, N. Ao, W. K. Hocking, T. Sato, M. Yamamoto, T. Nakamura, T. Tsuda, and S. Kato (1994), Seasonal variability of vertical eddy diffusivity in the middle atmosphere 1. Three-year observations by the middle and upper atmosphere radar, *J. Geophys. Res.*, *99*(D9), 18,973–18,987, doi:10.1029/94JD00911.

Garcia, R. R., M. López-Puertas, B. Funke, D. E. Kinnison, D. R. Marsh, and L. Qian (2016), On the secular trend of CO_x and CO_2 in the lower thermosphere, *J. Geophys. Res. Atmos.*, *121*, 3634–3644, doi:10.1002/2015JD024553.

Gardner, C. S., and A. Z. Liu (2007), Seasonal variations of the vertical fluxes of heat and horizontal momentum in the mesopause region at Starfire Optical Range, New Mexico, *J. Geophys. Res.*, *112*, D09113, doi:10.1029/2005JD006179.

Gardner, C. S., and A. Z. Liu (2014), Measuring eddy heat and constituent fluxes with high-resolution Na and Fe Doppler lidars, *J. Geophys. Res.*, *119*, 10,583–10,603, doi:10.1002/2013JD021074.

Gardner, C. S., and A. Z. Liu (2016), Chemical transport of neutral atmospheric constituents by waves and turbulence: Theory and observations, *J. Geophys. Res. Atmos.*, *121*, 494–520, doi:10.1002/2015JD023145.

Gardner, C. S., and W. Yang (1998), Measurements of the dynamical cooling rate associated with the vertical transport of heat by dissipating gravity waves in the mesopause region at the Starfire Optical Range, New Mexico, *J. Geophys. Res.*, *103*(D14), 16,909–16,926.

Gardner, C. S., C. A. Hostetler, and S. Lintelman (1993), Influence of the mean wind field on the separability of atmospheric perturbation spectra, *J. Geophys. Res.*, *98*(D5), 8859–8872.

Gavrilov, N. M., H. Luce, M. Crochet, F. Dalaudier, and S. Fukao (2005), Turbulence parameter estimations from high-resolution balloon temperature measurements of the MUTSI-2000 campaign, *Ann. Geophys.*, *23*(7), 2401–2413.

Hall, C. M., U. P. Hoppe, T. A. Blix, E. V. Thrane, A. H. Manson, and C. E. Meek (1999), Seasonal variation of turbulent energy dissipation rates in the polar mesosphere: A comparison of methods, *Earth Planets Space*, *51*(7), 515–524, doi:10.1186/BF03353212.

Hecht, J. H., K. Wan, L. J. Gelinas, D. C. Fritts, R. L. Walterscheid, R. J. Rudy, A. Z. Liu, S. J. Franke, F. A. Vargas, P. D. Pautet, M. J. Taylor, and G. R. Swenson (2014), The life cycle of instability features measured from the Andes Lidar Observatory over Cerro Pachón on 24 March 2012, *J. Geophys. Res. Atmos.*, *119*, 8872–8898, doi:10.1002/2014JD021726.

Heck, W. J., H. A. Panofsky, and M. A. Bender (1977), The effect of clear-air turbulence on a model of the general circulation of the atmosphere, *Beitr. Phys. Atmos.*, *50*, 89–97.

Hickey, M. P., R. L. Walterscheid, and G. Schubert (2011), Gravity wave heating and cooling of the thermosphere: Sensible heat flux and viscous flux of kinetic energy, *J. Geophys. Res. Space*, *116*, A12326, doi:10.1029/2011JA016792.

Hines, C. O. (1991), The saturation of gravity waves in the middle atmosphere. Part II: Development of doppler-spread theory, *J. Atmos. Sci.*, *48*(11), 1361–1379, doi:10.1175/1520-0469(1991)048<1361:TSOGWI>2.0.CO;2.

Hocking, W. K. (1996), An assessment of the capabilities and limitations of radars in measurements of upper atmosphere turbulence, *Adv. Space Res.*, *17*(11), 37–47, doi:10.1016/0273-1177(95)00728-W.

Hodges, R. R. (1969), Eddy diffusion coefficients due to instabilities in internal gravity waves, *J. Geophys. Res.*, *74*(16), 4087–4090.

Krueger, D. A., C.-Y. She, and T. Yuan (2015), Retrieving mesopause temperature and line-of-sight wind from full-diurnal-cycle Na lidar observations, *Appl. Opt.*, *54*(32), 9469–9489.

Larsen, M. F., J. Rutger, and D. N. Holden (1987), Direct measurements of vertical-velocity power spectra with the SOUSY-VHF-Radar wind profiler system, *J. Atmos. Sci.*, *44*(23), 3442–3448, doi:10.1175/1520-0469(1987)044<3442:DMOVVP>2.0.CO;2.

Lindzen, R. S. (1981), Turbulence and stress owing to gravity wave and tidal breakdown, *J. Geophys. Res.*, *86*, 9707–9714.

Liu, A. Z., R. G. Roble, J. H. Hecht, M. F. Larsen, and C. S. Gardner (2004), Unstable layers in the mesopause region observed with Na lidar during the Turbulent Oxygen Mixing Experiment (TOMEX) campaign, *J. Geophys. Res.*, *109*, D02S02, doi:10.1029/2002JD003056.

Liu, A. Z., Y. Guo, F. Vargas, and G. R. Swenson (2016), First measurement of horizontal wind and temperature in the lower thermosphere (105–140 km) with a Na Lidar at Andes Lidar Observatory, *Geophys. Res. Lett.*, *43*, 2374–2380, doi:10.1002/2016GL068461.

Liu, H.-L. (2000), Temperature changes due to gravity wave saturation, *J. Geophys. Res.*, *105*(D10), 12,329–12,336.
Lu, X., X. Chu, W. Fong, C. Chen, Z. Yu, B. R. Roberts, and A. J. McDonald (2015), Vertical evolution of potential energy density and vertical wave number spectrum of Antarctic gravity waves from 35 to 105 km at McMurdo (77.8°S, 166.7°E), *J. Geophys. Res. Atmos.*, *120*, 2719–2737, doi:10.1002/2014JD022751.
Lübken, F.-J. (1997), Seasonal variation of turbulent energy dissipation rates at high latitudes as determined by in situ measurements of neutral density fluctuations, *J. Geophys. Res.*, *102*(D12), 13,441–13,456.
Lübken, F.-J., U. von Zahn, E. Thrane, T. Blix, G. Kokin, and S. Pachomov (1987), In situ measurements of turbulent energy dissipation rates and eddy diffusion coefficients during MAP/WINE, *J. Atmos. Terr. Phys.*, *49*(7-8), 763–775.
Meraner, K., and H. Schmidt (2016), Transport of nitrogen oxides through the winter mesopause in Hammonia, *J. Geophys. Res. Atmos.*, *121*, 2556–2570, doi:10.1002/2015JD024136.
Papen, G. C., W. M. Pfenninger, and D. M. Simonich (1995), Sensitivity analysis of Na narrowband wind-temperature lidar systems, *Appl. Opt.*, *34*(3), 480–498.
Qian, L., S. C. Solomon, and T. J. Kane (2009), Seasonal variation of thermospheric density and composition, *J. Geophys. Res.*, *114*, D09301, doi:10.1029/2008JA013643.
Sasi, M. N., and L. Vijayan (2001), Turbulence characteristics in the tropical mesosphere as obtained by MST radar at Gadanki (13.5°N, 79.2°E), *Ann. Geophys.*, *19*(8), 1019–1025.
Senft, D. C., and C. S. Gardner (1991), Seasonal variability of gravity wave activity and spectra in the mesopause region at Urbana, *J. Geophys. Res.*, *96*(D9), 17,229–17,264.
Smith, A. K. (2012), Global dynamics of the MLT, *Surv. Geophys.*, *33*(6), 1177–1230, doi:10.1007/s10712-012-9196-9.
Smith, J. A., and X. Chu (2015), High-efficiency receiver architecture for resonance-fluorescence and Doppler lidars, *Appl. Opt.*, *54*(11), 3173–3184.
Tatarskii, V. I. (1971), The effects of the turbulent atmosphere on wave propagation, in *Jerusalem: Israel Program for Scientific Translations*, p. 472, Reproduced by National Technical Information Service, U.S. Dept. of Commerce, Springfield, Va.
VanZandt, T. E., G. D. Nastrom, and J. L. Green (1991), Frequency spectra of vertical velocity from Flatland VHF radar data, *J. Geophys. Res. Atmos.*, *96*(D2), 2845–2855, doi:10.1029/90JD02220.
Vlasov, M. N., and M. C. Kelley (2014), Criterion for analyzing experimental data on eddy diffusion coefficients, *Ann. Geophys.*, *32*(6), 581–588, doi:10.5194/angeo-32-581-2014.
Vlasov, M. N., and M. C. Kelley (2015), Eddy diffusion coefficients and their upper limits based on application of the similarity theory, *Ann. Geophys.*, *33*(7), 857–864, doi:10.5194/angeo-33-857-2015.
Walterscheid, R. L. (1981), Dynamical cooling induced by dissipating internal gravity waves, *Geophys. Res. Lett.*, *8*(12), 1235–1238.
Weinstock, J. (1978), Vertical turbulent diffusion in a stably stratified fluid, *J. Atmos. Sci.*, *35*(6), 1022–1027.
Weinstock, J. (1981), Energy dissipation rates of turbulence in the stable free atmosphere, *J. Atmos. Sci.*, *38*(4), 880–883.
Weinstock, J. (1990), Saturated and unsaturated spectra of gravity waves and scale-dependent diffusion, *J. Atmos. Sci.*, *47*(18), 2211–2226, doi:10.1175/1520-0469(1990)047<2211:SAUSOG>2.0.CO;2.
Williams, B. P., D. C. Fritts, J. D. Vance, C. Y. She, T. Abe, and E. Thrane (2006), Sodium lidar measurements of waves and instabilities near the mesopause during the DELTA rocket campaign, *Earth Planets Space*, *58*(9), 1131–1137.
Zhang, S. D., F. Yi, C. M. Huang, and K. M. Huang (2012), High vertical resolution analyses of gravity waves and turbulence at a midlatitude station, *J. Geophys. Res.*, *117*, D02103, doi:10.1029/2011JD016587.
Zhang, X., J. M. Forbes, M. E. Hagan, J. M. Russell III, S. E.Palo, C. J. Mertens, and M. G. Mlynczak (2006), Monthly tidal temperatures 20–120 km from TIMED/SABER, *J. Geophys. Res.*, *111*, A10S08, doi:10.1029/2005JA011504.
Zhao, Y., A. Z. Liu, and C. S. Gardner (2003), Measurements of atmospheric stability in the mesopause region at Starfire Optical Range, NM, *J. Atmos. Sol. Terr. Phys.*, *65*, 219–232.
Zhu, X., J.-H. Yee, W. H. Swartz, E. R. Talaat, and L. Coy (2010), A spectral parameterization of drag, eddy diffusion, and wave heating for a three-dimensional flow induced by breaking gravity waves, *J. Atmos. Sci.*, *67*(8), 2520–2536.